ADVANCED FUNCTIONAL MATERIALS
www.afm-journal.de

High Efficiency and High Open Circuit Voltage in Quasi 2D Perovskite Based Solar Cells

*Bat-El Cohen, Małgorzata Wierzbowska, and Lioz Etgar**

An important property of hybrid layered perovskite is the possibility to reduce its dimensionality to provide wider band gap and better stability. In this work, 2D perovskite of the structure $(PEA)_2(MA)_{n-1}Pb_nBr_{3n+1}$ has been sensitized, where PEA is phenyl ethyl-ammonium, MA is methyl-ammonium, and using only bromide as the halide. The number of the perovskite layers has been varied (n) from $n = 1$ through $n = \infty$. Optical and physical characterization verify the layered structure and the increase in the band gap. The photovoltaic performance shows higher open circuit voltage (V_{oc}) for the quasi 2D perovskite (i.e., $n = 40, 50, 60$) compared to the 3D perovskite. V_{oc} of 1.3 V without hole transport material (HTM) and V_{oc} of 1.46 V using HTM have been demonstrated, with corresponding efficiency of 6.3% and 8.5%, among the highest reported. The lower mobility and transport in the quasi 2D perovskites have been proved effective to gain high V_{oc} with high efficiency, further supported by ab initio calculations and charge extraction measurements. Bromide is the only halide used in these quasi 2D perovskites, as mixing halides have recently revealed instability of the perovskite structure. These quasi 2D materials are promising candidates for use in optoelectronic applications that simultaneously require high voltage and high efficiency.

1. Introduction

Organic–inorganic perovskites are being used today in a variety of optoelectronic applications.[1–5] In particular, methyl-ammonium (MA) lead iodide ($MAPbI_3$) perovskite shows a large absorption coefficient, long-range photocarrier diffusion lengths, and a suitable band gap. To date, the certified power conversion efficiency (PCE) of these solar cells is 22.1%.[6]

The organic–inorganic perovskite is formed as quantum well system where the organic cations act as a barrier while the metal halide form quantum wells.[7] Typically the organic cation has low dielectric constant while the metal halide has higher dielectric constant. The organic–inorganic perovskite configuration is of the structure $R_2(CH_3NH_3)_{n-1}M_nX_{3n+1}$, where R is an organic group, M is a divalent metal, and X is a halide (Cl^-, Br^-, or I^-). The number of perovskite layers are determined by the long organic groups separated by the MX_6 layers.[8] In this work, quasi 2D perovskites were synthesized which could involve a mixing of 2D and 3D perovskite in the same film. When reducing dimensionality, the exciton binding energy increased up to 300 meV for typical 2D organic–inorganic perovskite; in addition, the excitons are expected to be more stable in low dimension perovskites. This family of materials permits tuning of optical and electrical properties by changing either the organic or the inorganic component, or their relative abundance.

There are two main options to tune the organic–inorganic perovskite band gap: (i) Creating a confinement in the perovskite structure, such as reducing dimensionality. When moving from pure 3D perovskite to 2D perovskite, the band gap increases. (ii) Changing the halides in the perovskite structure to bromide to increase the perovskite band gap.[9]

Cao et al. used the butylammonium as the barrier to create low dimensional perovskites using the iodide as the halide starting from $n = 1$ (single perovskite layer) to $n = 4$; however, the photovoltaic (PV) performance of these cells was low, mainly due to transport problems.[10] Quan et al. fabricated reduced dimensionality in the perovskite structure using the iodide as well, where low n values and high n values were studied. It was shown that the high n values could provide better stability than the 3D perovskite.[11] Several studies show the use of 3D perovskite based bromide in high voltage cells having open circuit voltage ranging from 1.15–1.5 V.[12–17] Moreover, high voltage (1.4 V) and high efficiency (6.7%) were reported with hole transport material (HTM) based on tri-arylamine polymer derivatives containing fluorene and indenofluorene.[18] High voltage was also observed for cells without a hole conductor; however, the efficiency was still low.[19,20] Recently, $MAPbBr_3$ perovskite with more than 10% efficiency was reported for planar configuration.[21]

In this work, we demonstrate the combination of the two effects that increase the perovskite band gap, i.e., reduced dimensionality and use of bromide in the perovskite structure. Quasi 2D perovskite (high n values) from the structure

B.-E. Cohen, Dr. L. Etgar
The Hebrew University of Jerusalem
Institute of Chemistry
Casali Center for Applied Chemistry
Jerusalem, Israel
E-mail: lioz.etgar@mail.huji.ac.il
Dr. M. Wierzbowska
Institute of Physics
Polish Academy of Sciences
Aleja Lotnikow 32/46, PL-02-668 Warsaw, Poland

DOI: 10.1002/adfm.201604733

$(PEA)_2(MA)_{n-1}Pb_nBr_{3n+1}$ were synthesized (PEA corresponds to phenyl ethyl ammonium). The numbers of layers (n) which determine the perovskite dimensionality were changed in the range of $1 \le n \le \infty$. Absorbance, photoluminescence (PL), PL-lifetime, X-ray diffraction (XRD), scanning electron microscopy (SEM), and optical microscopy were used for detailed characterization of the various layered perovskites. Solar cells with and without hole conductor were fabricated using the layered perovskite demonstrating high V_{oc} with high efficiency. Higher V_{oc} was demonstrated for the quasi 2D perovskite compared to the 3D perovskite. The density functional theory (DFT) method and the Wannier-function based postprocessing for solving the Boltzmann-type equations were used to show the change in conductivity when changing the dimensionality of the perovskite. Finally, charge extraction measurements were applied to understand the PV behavior of these quasi 2D perovskites.

2. Results and Discussion

Figure 1 shows the dimensionality in the perovskite structure according to the formula $(PEA)_2(MA)_{n-1}Pb_nBr_{3n+1}$ (where PEA is phenylethyl ammonium and MA is methylammonium) yielding compounds with different layer (n) values (i.e., n = 1, 2,...., ∞). Consequently, $n = \infty$ is cubic 3D perovskite such as $MAPbBr_3$, while the other n values describe 2D (n = 1) or quasi-2D ($n > 1$) perovskite structure.

We fabricated dimensional perovskite films using the PEA as a barrier to tune the dimensions of the perovskite. The number of perovskite layers (n) was varied from n = 1 to n = 60 and $n = \infty$, which is the 3D perovskite. The absorbance spectra of the various n values are shown in Figure S1A in the Supporting Information for $1 \le n \le 10$ and in **Figure 2**A for $20 \le n \le \infty$. At low n values the perovskite energy band gap (Eg) decreases, starting from Eg = 3 eV for n = 1 (described by the formula $(PEA)_2(MA)PbBr_4$) through Eg = 2.3 eV for n = 10 (described by the formula $(PEA)_2(MA)_9Pb_{10}Br_{28}$). It was previously reported that low n values provide much more stable perovskite structures compared to their 3D perovskite counterparts.[10] However, their transport properties are not as good as the 3D perovskite (the PV performance of low n values are discussed below). Therefore, we were motivated to fabricate higher n values in order to have good perovskite stability[10] but with transport properties close to the 3D perovskite (referred to as quasi-2D). Figure 2A presents the absorbance of high n values (i.e., 40, 50, 60, and ∞). It can be seen that the absorbance onset almost does not change at these high n values, similar to the description by Quan et al.[10] indicating similar Eg at high n values. The absorbance spectra of the quasi 2D perovskite (n = 40, 50, and 60) have more prominent exitonic feature which suggest on lower dimensionality in these samples.[22] The corresponding exciton-binding energies estimated from these plots according to Elliott formula[23,24] are 56 meV for n = 40, 54 meV for n = 50, 62.5 meV for n = 60, and 54 meV for $n = \infty$ (Figure S9 in the Supporting Information). In addition, the energy difference between the band gap and the PL is very small, in the order of several dozen meV, providing a rough estimation of the exciton binding energy (Figure 2B inset). The strong PL at these quantum well structures is observed due to stable excitons in the 2D perovskites as a result of the coulombic charge screening effect.[25] At generation, the exciton is strongly confined between the positive organic spacers and the negative inorganic perovskite, inhibiting the exciton splitting into free carriers. Furthermore, the broad PL might be related to trap states in these materials. The PL lifetime is presented in Figure 2B, where the 3D perovskite ($MAPbBr_3$) shows a shorter PL lifetime than the quasi-2D perovskites (i.e., n = 40, 50, 60). The life time values are presented in Table S2 (Supporting Information). These results demonstrate a longer lifetime for the quasi 2D perovskites compared to the 3D perovskite (in good agreement with the charge extraction measurements discussed below), supporting the better open circuit voltage of these cells, described below.

The layered perovskite consists of a corner sharing $(PbI_6)^-$octahedra in two directions while the third direction is related to the octahedral sheets, separated using organic bilayers. In the case of 2D perovskite, the layers will grow thicker by introducing the small MA cation; therefore, the perovskite unit cell expands by introducing a single perovskite layer one at a time. The changes in the unit cell are detected by XRD where low angle reflections are observed when adding a single perovskite layer.[21] The low angle reflections that indicate the addition of unit cells are below ≈2Ø = 15°. The reason for the cut off at 15° is because both the discrete layers match their d-spacing at the 3D perovskite reflection (110) and at the 2D perovskite reflection (111).[21] Based on this, **Figure 3**A shows the XRD pattern for the high n values including n = 1. In the case of n = 1, there is no reflection peak at 2Ø = 15° indicating pure 2D perovskite. When looking at the low angles in the XRD pattern, a reflection is observed at ≈5.3° for n = 1, 20, 40, 50, and 60; see the inset of Figure 3A. No reflection was observed for $n = \infty$, which supports the 2D nature of these samples. Worth noting, since these are quasi-2D perovskite including many of the 3D perovskite layers, we assume that mixing of 3D and 2D perovskites is present in the same sample. Figure S1B (in the Supporting Information) shows the XRD pattern of the 2D perovskite with low n values, in contrast to the high n values; more reflections are observed at low angles (i.e., below 2Ø = 15°), indicating that at low n values, the 2D nature is more pronounced, compared to the 3D perovskite.

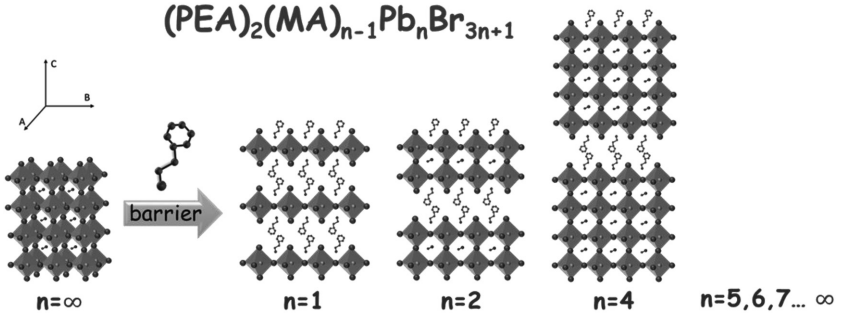

Figure 1. Schematic illustration of different dimensions in the organic–inorganic perovskite structure. The barrier is phenyl-ethyl-ammonium bromide (PEABr).

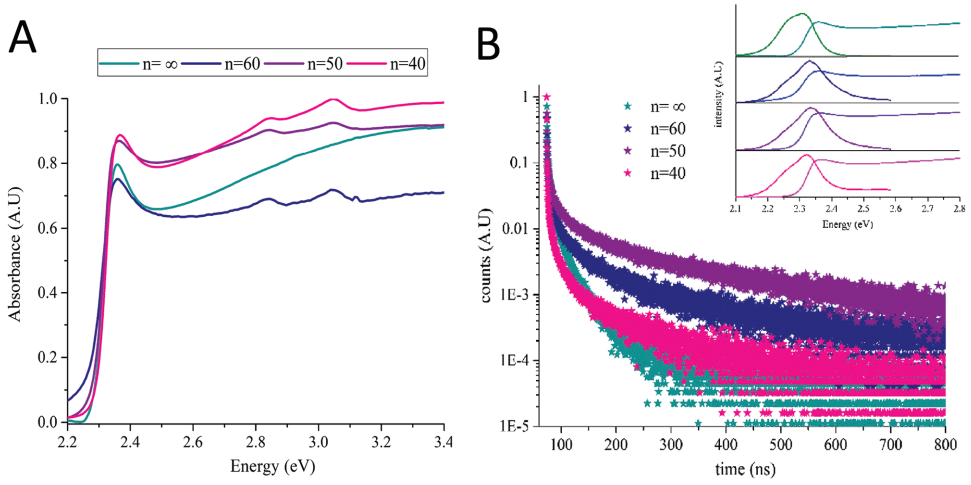

Figure 2. A) Absorbance spectra of $n = 40$, 50, 60 and $n = \infty$; B) PL lifetime of the corresponding samples ($n = 40$, 50, 60, ∞). Inset: PL and absorbance of the samples.

Figure 3B,C presents optical microscope images of $n = 20$ $[(PEA)_2(MA)_{19}Pb_{20}Br_{61}]$ and $n = \infty$ $[MAPbBr_3]$. The difference is clearly detected where the platelets nature of the $n = 20$ sample is seen, while in the case of the 3D sample ($n = \infty$), more thick crystals with tetragonal/cubic shape are seen. This is further supported by the SEM images of $n = 20$ and $n = \infty$, Figure 3D,E, respectively. The surface in Figure 3E is covered by large cubic crystals, while the surface in the case of $n = 20$ is mainly rough crystals with layered character structure, can be also seen at the inset of Figure 3D.

The PV performance of the 2D and the quasi-2D perovskites was evaluated. As described, the 2D and the quasi-2D perovskites are based on bromide, resulting in an increase of the band gap compared to the iodide counterpart. A large band gap could potentially provide higher open circuit voltage (V_{oc}). In addition, the solar cell structure used in this work is based on our previous reports[26,27] where no HTM was used. Not using HTM simplified the solar cell structure and could enhance the stability and reduce the solar cell cost. Our aim in this work is to demonstrate high V_{oc} and high PCE without HTM using the quasi-2D perovskites.

Figure 4A shows a schematic illustration of the solar cell structure eliminating the use of HTM. The pure 2D perovskite and the low n values (up to $n = 10$) were tested in this solar cell configuration. The PV results are presented in Table S1 in the Supporting Information indicating very low PV performance, mainly due to reduced mobility and lower lifetime[28] Moreover, the wider band gap of these low n values also prevents them from absorbing longer wavelengths, which reduces their PV performance. Figure S2 in the Supporting Information shows representative top view SEM images of the different n values deposited on the mesoporous TiO_2; the film coverage is very good in all cases, supporting the fact that the low PCE is mainly due to transport properties of the layered perovskite

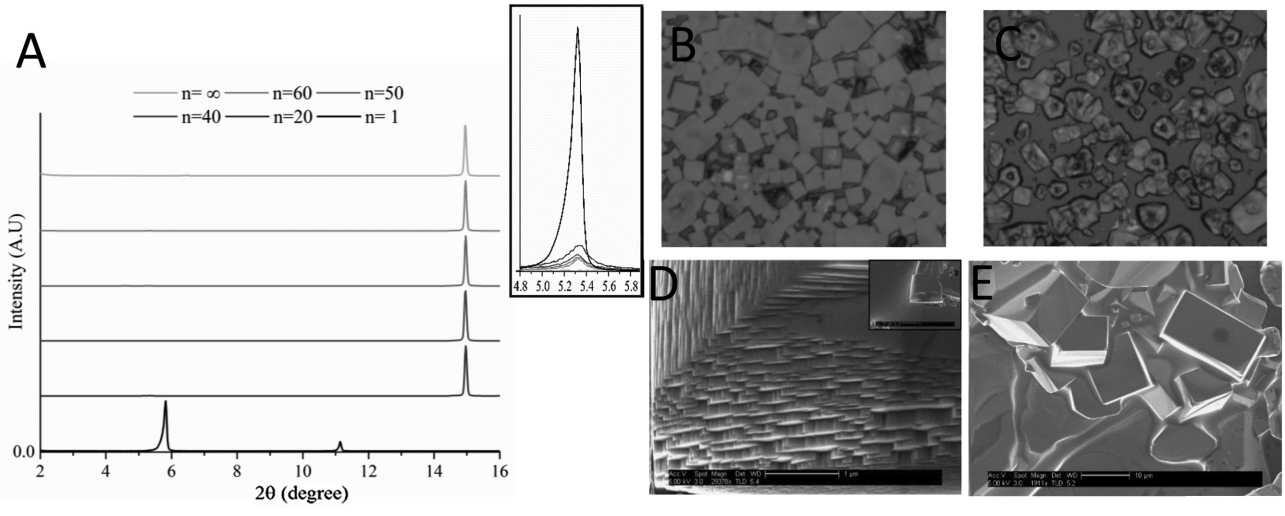

Figure 3. A) XRD pattern of $n = 1$, 20, 40, 50, 60, and ∞. Inset: magnification of the peaks observed at ≈5.3° for $n = 1$, 20, 40, 50, and 60, while no reflection was observed for $n = \infty$. The full XRD can be observed in Figure S1C (Supporting Information). B,C) Optical microscopy images of $n = 20$ and $n = \infty$, respectively. D,E) SEM images of $n = 20$, scale bar = 5 µm (inset scale bar = 1 µm) and $n = \infty$, scale bar = 10 µm, respectively.

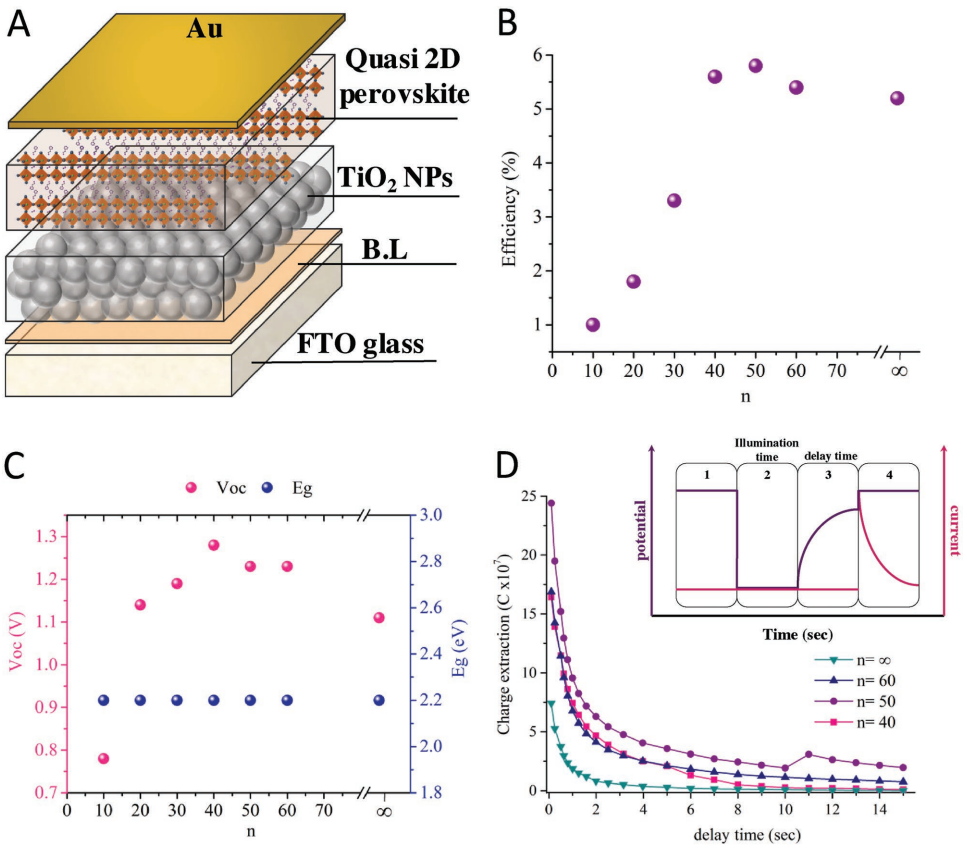

Figure 4. A) Solar cell configuration studied in this manuscript. B) PCE as a function of the *n* values. C) V_{oc} and energy gap as a function of the *n* values. D) Charge extraction measurements of the various *n*. Inset: Various stages in the charge extraction measurements.

with low *n* values. The average PV performance of the quasi-2D perovskites (high *n* values) is presented in **Table 1** and Figure 4B,C. (≈60 cells were fabricated for $n = 40$, 50, and 60). The PCE increases with *n* values, with maximum PCE of 5.8% ± 0.2 for $n = 50$, while the PCE decreases for higher *n* values as well as for the 3D structure. The V_{oc} of the cells behaves similarly, where the highest V_{oc} is 1.28 V± 0.02 for $n = 40$, while the V_{oc} decreases for higher *n* values and for the 3D perovskite. As mentioned, the energy gap does not change from $n = 10$ to $n = \infty$; therefore, we would expect that the V_{oc} will not be affected as a result of the change in the *n* values. However, as observed in Figure 4C and Table 1, there is a clear change in V_{oc} for different *n* values. It is important to note that the V_{oc} for $n = 40$, $n = 50$ and $n = 60$ is significantly higher than the V_{oc} of $n = \infty$ and $n = 20$, 30. The V_{oc} is mainly related to the mobility; high V_{oc} indicates a decrease in mobility. As stated, the mobility is lower for the 2D and the quasi-2D perovskite compared to the 3D perovskite. Mitzi et al. reported a decrease in conductivity when reducing dimensionality.[29] When the mobility is lower, fewer charges will be accumulated at the selective contacts resulting in better charge extraction and less recombination.

Table 1. Average PV parameters of the large *n* values. All results are for HTM free cells.

n $(PEA)_2(MA)_{n-1}Pb_nBr_{3n+1}$	V_{oc} [V]	J_{sc} [mA cm^{-2}]	FF	Efficiency [%]
$n = \infty$	1.11 ± 0.06	8.1 ± 0.6	58 ± 4	5.2 ± 0.6
$n = 60$	1.23 ± 0.03	8.1 ± 0.8	55 ± 5	5.4 ± 0.3
$n = 50$	1.23 ± 0.02	8.3 ± 0.6	57 ± 2	5.8 ± 0.2
$n = 40$	1.28 ± 0.01	7.9 ± 0.4	56 ± 5	5.6 ± 0.4
$n = 30$	1.11 ± 0.07	5.7 ± 0.8	51 ± 5	3.2 ± 0.5
$n = 20$	1.16 ± 0.10	4.4 ± 0.9	46 ± 3	2.4 ± 0.6

In order to observe the increase in conductivity when increasing dimensionality, we performed the DFT calculations of the electronic structure and solved the Boltzmann equations using bands accurately interpolated with the post-processing code based on the Wannier functions. To numerically model the quasi 2D perovskite (i.e., with several dozens of perovskite layers), we simulated the case for $n = 4$ as a reference (called P1). Then we assumed that when introducing more perovskite layers, pressure was induced between the phenyl rings. This effect increased the π–π type overlap between the rings which, in turn, changed the conductivity in the regions between the perovskite layers. Figure S4 (in the Supporting Information) illustrates the decrease of spacing in the PEA layers due to the increase in pressure, as a result of the additional perovskite layers.

The three simulated structures with the growing effect of pressure are called P1 (no pressure), P2 (middle pressure), and P3 (highest pressure, complete overlap of rings) and are depicted in **Figure 5**.

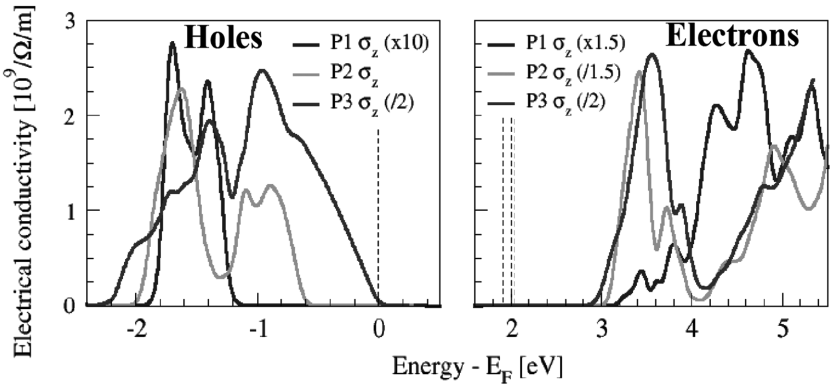

Figure 5. Electrical conductivity for electrons (right) and holes (left) as was calculated. The energies are relative to the Fermi level, i.e., the VBT, marked with black dashed line. The energy gaps of the three cases differ a little—the CBM is at 2.01, 2.03, and 1.93 eV for P1, P2, and P3, respectively; marked with corresponding blue, green, and red dashed lines.

Growing overlap of the phenyl rings in the *XZ*-plane causes an increase of the electrical conductivity across the layered perovskite (in the *Z* direction), displayed in Figure 5 for the holes and electrons. All energies are relative to the Fermi level, i.e., valence band top (VBT), marked with a black dashed line. The energy gaps of the three cases differ—the conduction band minimum (CBM) for P1, P2, and P3 is marked with corresponding blue, green, and red dashed lines. Some curves are resized, according to the legends, to present them on the same scale; therefore, it can be seen that the highest conductivity is observed for P3 compared to P2 and the lowest is P1. In addition, the onset of the conductivity moves toward the VBT for holes and toward CBM for electrons. This means that generation of an electron-hole pair in the phenyl ring region consumed less energy for P3 than for P2 and P1. (i.e., when increasing the number of perovskite layers, less energy is required to generate electrons and holes in the PEA layers of the heterostructure).

Moreover, the width and energetic position of the conductivity curves correspond to the bandwidth and position of the bands projected onto the phenyl ethylammonium—see the bands along G-Z and M-A symmetry lines and the electrical conductivities in Figures S5–S7 in the Supporting Information. For comparison, the electrical conductivities and band structures within the planes of the three cases (P1, P2, and P3) are presented in Figures S5–S7 in the Supporting Information.

Charge extraction, mainly used in sensitized solar cells,[26] is an important tool for studying electron transport, recombination rate and interfacial transfer.[30] The inset of Figure 4D shows the steps involved in the charge extraction (CE) method used in this work. The steps include: (1) A two-second step in which the cell is discharged in the dark; (2) The cell is then disconnected and illuminated for 2 s (illumination time); (3) The light is then switched off and the system waits a specified time called delay time. In this step, a charge recombination occurs inside the cell; (4) The cell is reconnected, and the charges that remain and did not recombine are extracted and measured. This process is repeated for different delay times, from 0.5 to 15 s. The CE measurements (presented in Figure 4D) show that in the case of the quasi-2D perovskite, more charges are left to extract (for a specified delay time), compared to the 3D perovskite, where fewer charges are extracted (for the same delay time). This is an indication that the recombination rate in the case of quasi-2D perovskites is lower than the recombination rate of the 3D perovskite. This conclusion is based on the fact that during step 3 (delay time) recombination occurs inside the cell (mainly in the perovskite and at the selective contacts) and the charges that remain (and will be extracted) are dependent on the rate of recombination. The CE results support the higher V_{oc} observed for the quasi-2D perovskite (n = 40, 50 and 60) compared to the 3D perovskite. These results are consistent with the electronic density maps obtained by means of the DFT for the P1, P2 and P3 structures, for the electron and hole doped cells; presented in Figure S8 in the Supporting Information. Both electrons and holes are located at the PbI_6 frame and not much on the MA and PEA. However, the electrons are located mostly at the surface of the perovskite and the holes are located in the "bulk." Therefore, in case of charge accumulation at the PEA/$MAPbBr_3$ interfaces, the time decrease of the capacitance is expected to be faster (in the units C s^{-1}) for lower n values, due to smaller separation between hole- and electron-rich regions. Moreover, an amount of the total accumulated charge should be larger for higher n values (more heterostructures in the device). Although, the charge per PEA/$MAPbBr_3$ interface might be a bit smaller for lower n—due to partial accumulation of holes at the same region where the electrons mostly localize in the case of small pressure, i.e., P1. In addition to the charge extraction measurements and the DFT calculations, the PL lifetime presents shorter lifetime for the 3D perovskite than for n = 50 which has longer lifetime than n = 60 and n = 40. (Table S2, Supporting Information) These results are in partial agreement with the V_{oc} of the corresponding cells. Therefore, we can conclude that the V_{oc} is not determining only by the number of perovskite layers and that the selective contacts also play a role in determined the V_{oc} of the cells.

Table 2 and **Figure 6** present the best *P*–*V* parameters and the *I*–*V* curves of the various HTM free solar cells. The 3D perovskite ($MAPbBr_3$) shows high PCE of 6.2% with V_{oc} of 1.14 V; n = 60 shows slightly better PCE with much higher V_{oc} of 1.25 V. Figure S3A in the Supporting Information shows the current versus time of this cell indicating that the measurement was taken after the cell stabilized. The best V_{oc} was observed for

Table 2. Best-performing cells observed for HTM free configuration and with Spiro as HTM.

n $(PEA)_2(MA)_{n-1}Pb_nBr_{3n+1}$	V_{oc} [V]	J_{sc} [mA cm^{-2}]	FF	Efficiency [%]
∞ (HTM free)	1.14	9.6	56	6.2
60 (HTM free)	1.25	8.2	62	6.3
40 (HTM free)	1.30	8.4	50	5.5
50 + Spiro	1.46	9.0	65	8.5
∞ + Spiro	1.22	10.7	66	8.1

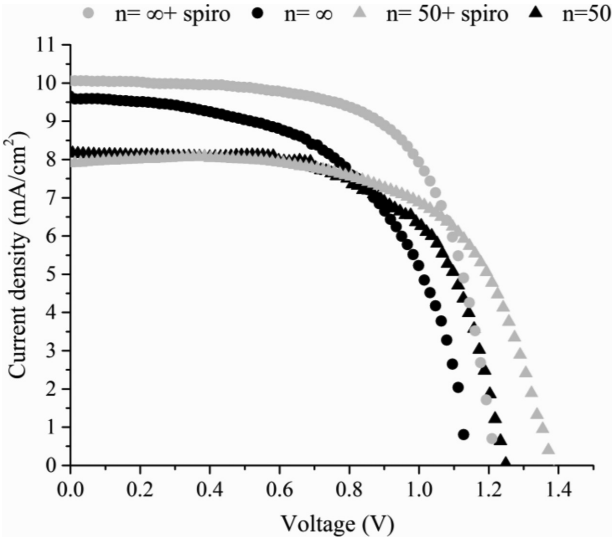

Figure 6. *J–V* curves of the best-performing cells observed for quasi-2D and 3D perovskite with and without HTM.

the $n = 40$ perovskite ($(PEA)_2(MA)_{39}Pb_{40}Br_{121}$) attaining 1.3 V for the HTM free cell.

To see how high the PCE could increase and, in addition, to compare it to our HTM free cells, we fabricated the same cells with Spiro as the HTM. As presented in Table 2 and Figure 6, the best PCE was observed for $n = 50$ ($(PEA)_2(MA)_{49}Pb_{50}Br_{151}$) achieving 8.5% with V_{oc} of 1.46 V. To the best of our knowledge, the PCE and the V_{oc} achieved in this study for HTM free cells and for cells with Spiro are among the highest reported. (All the perovskites studied are based only on bromide). The hysteresis curves of the 3D perovskite and the various n values (i.e., $n = 60$, 50, and 40) are presented in Figure S3B–E (Supporting Information), respectively. The smallest hysteresis is observed for the 3D perovskite; the hysteresis is pronounced when reducing the n values. This phenomenon is still not clear to us; however, it can be explained through the decrease in conductivity while reducing n values (as previously discussed). The lower conductivity, for example, for $n = 40$ compared to $n = \infty$, could result in more charge accumulation at the selective contacts as observed theoretically—which, in turn, might affect the hysteresis. This interesting phenomenon will be investigated further in a following study.

3. Conclusions

This work demonstrates the synthesis of 2D and 3D layered perovskites and their PV activity. PEA was used as the barrier molecule in order to get various perovskite layers starting from $n = 1$ (for pure 2D perovskite) through $n = \infty$ (for 3D perovskite). XRD measurements showed the nature of the 2D perovskite indicated by the low angle reflections. Absorbance and PL proved the confinement effect by the change in the band gap. PV solar cells with HTM and without HTM were fabricated demonstrating high open circuit voltage and high PCE for the quasi-2D perovskite ($n = 40$, 50, 60) compared to the 3D perovskite. The lower mobility and transport in the quasi 2D perovskites is beneficial to the solar cell performance, in particular, to achieve high V_{oc}. This fact was supported by charge extraction measurements. Moreover, the DFT simulations show an increase of the electrical conductivity when increasing the perovskite dimensionality, further supporting the PV performance of these cells. This work shows that the quasi-2D perovskites are attractive candidates for high voltage and high efficiency solar cells.

4. Experimental Section

Perovskite Precursor Synthesis: Synthesis of methylammonium bromide (MABr) was done by reacting 29 mL of methylamine (40% in methanol, TCI) with 100 mL of hydrobromic acid (48 wt% in water, Aldrich) in a 250 mL round bottom flask at 0 °C for 2 h with stirring. The solvent was removed in a rotary evaporator at 50 °C for 1 h and the precipitate was collected. This precipitate was filtered and washed with diethyl ether repeatedly for three times, and the white solid was collected and dried at 60 °C in a vacuum oven for 24 h.

Synthesis of phenylethylammonium bromide (PEABr) was done dropwise: 15 mL of hydrobromic acid (48 wt% in water, Aldrich) into a stirring solution of 10 mL of phenylethylammonium dissolved in 10 mL of ethanol absolute at 0 °C. After the addition of acid, the precipitate was left for 20 min at the same temperature. The precipitate was washed three times with diethyl ether and recrystallized twice with ethanol absolute.

Perovskite Solutions: $MAPbBr_3$ (corresponds for $n = \infty$) solution was prepared by dissolving equivalent amounts of MABr and $PbBr_2$ (Aldrich ≥ 98%) in 1:1 ratio of γ-butyrolactone (GBL): Dimethyl sulfoxide (DMSO) at 2 M concentration of each reagent.

Quasi 2D perovskite was prepared by dissolving stoichiometric quantity amounts of PEABr, MABr, and $PbBr_2$ according to the molecular formula of $(PEA)_2(MA)_{n-1}Pb_nBr_{3n+1}$ in 1:1 ratio of GBL:DMSO ($n \geq 10$) or in 4:1 ratio of dimethylformamide:DMSO ($n < 10$), at 2 M concentration of $PbBr_2$.

Device Fabrication: The TiO_2 nanoparticles (20 nm, dyesol) were diluted 1:4 ratio in ethanol and spin coated (5000 rpm, 30 s) onto a substrate with the following architecture of SnO2:F(FTO) conductive glass (15 O cm^1, Pilkington) coated by a layer of compact TiO_2 (TiDIP, 75% in isopropanol Aldrich). The substrate was then treated with $TiCl_4$. $(PEA)_2(MA)_{n-1}Pb_nBr_{3n+1}$ perovskite $10 \leq n < \infty$ solution was dropped on the substrate and spin coated in two-step 1000 and 5000 rpm for 10 and 60 s, respectively. During the second spin, 40 µL of toluene were deposited dropwise on the sample, for the last 30 s. $(PEA)_2(MA)_{n-1}Pb_nBr_{3n+1}$ perovskite $1 \leq n < 10$ the perovskite solution was dropped onto the substrate and spin coated for 5000 rpm for 30 s. The films were annealed at 100 °C for 1 h.

70 nm of gold electrode was thermally evaporated on the film under vacuum of $\approx 10^{-7}$ Torr.

Spiro Solution: 40 µL of 0.06 M 2,2′,7,7′-tetrakis-(*N*,*N*-di-4-methoxyphenylamino)-9,9′-spirofluorine (spiro-OMeTAD) in chlorobenzene with additives of 26.2 µL/1 mL bis(trifluoromethane)sulfonimide lithium salt in acetonitrile (520 mg mL^{-1}), 29.0 µL/1 mL tris(2-(1 H-pyrazol-1-yl)-4-tert-butylpyridine)-cobalt(III) tris(bis(trifluoromethylsulfonyl)imide)) in acetonitrile (300 mg mL^{-1}) and 19.2 µL/1 mL of 4-tert-butilpyridine (Aldrich) was spin coated at 4000 rpm for 30 s.

High-Resolution SEM (HR-SEM): The images were obtained using Sirion HR-SEM of FEI (Field Emission Instruments), The Netherlands. The measurement conditions were 5 kV at various magnifications, as seen on the data bar of the images.

Extra High-Resolution Scanning Electron Microscopy (XHRSEM): Magellan XHRSEM was performed using an FEI (Field Emission Instruments), The Netherlands. The measurement conditions were 5 kV.

Charge Extraction Measurements: Charge extraction measurements were done using AutolabPotentiostat-Galvenostat (PGSTAT) with FRA32M LED driver equipped with a white light source. The cells were illuminated from the substrate side. Nova 1.11 software program was used to collect and analyze the data obtained. A typical charge extraction experiment composed of (1) a 2 s step in which the cell was discharged in the dark; (2) the cell was then disconnected and illuminated for 2 s (illumination time); (3) the light was then switched off and the system waited a specified time called delay time. In this step, a charge recombination occurred inside the cell; (4) the cell was reconnected and the charges which remained and did not recombine were extracted and measured. This process was repeated for different delay times, from 0.5 to 15 s. The charges collected were plotted against delay time to provide insight on the lifespan of the charges after specified delay time.

Absorption Measurements: Absorption measurements were performed using Jasco V-670 spectrophotometer.

Photovoltaic Characterization: PV measurements were made on a New Port system, composed of an Oriel *I–V* test station using an Oriel Sol3A simulator. The solar simulator was class AAA for spectral performance, uniformity of irradiance, and temporal stability. The solar simulator was equipped with a 450 W xenon lamp. The output power was adjusted to match AM1.5 global sunlight (100 mW cm^{-2}). The spectral match classifications were IEC60904-9 2007, JIC C 8912, and ASTM E927-05. *I–V* curves were obtained by applying an external bias to the cell and measuring the generated photocurrent with a Keithley model 2400 digital source meter. The voltage step and delay time of photocurrent were 10 mV and 40 ms, respectively.

X-Ray Diffraction: XRD measurements were performed on the D8 Advance diffractometer (Bruker AXS, Karlsruhe, Germany) with a secondary graphite monochromator, 2° Soller slits, and a 0.2 mm receiving slit. XRD patterns within the range 2°–75° 2q were recorded at room temperature using CuKa radiation ($\lambda = 1.5418$ Å) with following measurement conditions: tube voltage of 40 kV, tube current of 40 mA, step-scan mode with a step size of 0.02° 2θ and counting time of 1 s per step.

PL and Time-Resolved PL Measurements: PL and time-resolved PL measurements were carried out in a time-correlated single-photon counting (TCSPC) approach using an Edinburgh Instruments FLS920 fluorescence spectrometer with a TCC900 TCSPC card. For time-resolved PL measurements, samples were excited using a Fianium WL-SC400-4-PP super continuum pulsed laser monochromatized at 410 nm. The emission from the sample was collected at a right angle, through long pass filter and a monochromator to suppress the scattering from excitation source, and collected using a Hamamatsu H10720 high speed PMT. PL measured from 520 to 600 nm with excitation wavelength of 450 nm. In order to extract the lifetime values, we used double-exponential decay fitting. The measurements were done for 1000 ns of decay reaching its baseline.

Details of the calculations are described in the Supporting Information.

Supporting Information

Supporting Information is available from the Wiley Online Library or from the author.

Acknowledgments

The authors would like to thank Israel Chemicals Ltd. Innovation for financial support to this work as well as the Tashtiot Project of the Office of the Chief Scientist. Thanks to Adam Faust for performing the PL lifetime measurements. Calculations were performed in the Cyfronet Computer Centre using Prometheus computer, which is a part of the PL-Grid Infrastructure. B.-E.C. preformed and planned the experiments and participated in the discussions. M.W. did the numerical simulations. L.E. planned the experiments, wrote the paper, and analyzed the results.

Received: September 12, 2016
Revised: October 17, 2016
Published online:

[1] M. M. Lee, J. Teuscher, T. Miyasaka, T. N. Murakami, H. J. Snaith, *Science* **2012**, *338*, 643.
[2] H. Kim, C. Lee, J. Im, K. Lee, T. Moehl, A. Marchioro, S. Moon, R. Humphry-Baker, J. Yum, J. Moser, M. Grätzel, N. Park, *Sci. Rep.* **2012**, *2*, 591.
[3] A. Kojima, K. Teshima, Y. Shirai, T. Miyasaka, *J. Am. Chem. Soc.* **2009**, *131*, 6050.
[4] N. Jeon, J. Noh, W. Yang, Y. Kim, S. Ryu, J. Seo, S. Seok II, *Nature* **2015**, *517*, 476.
[5] L. Etgar, P. Gao, Z. Xue, Q. Peng, A. K. Chandiran, B. Liu, Md. K. Nazeeruddin, M. Grätzel, *J. Am. Chem. Soc.* **2012**, *134*, 17396.
[6] http://www.nrel.gov/ncpv/images/efficiency_chart.jpg.
[7] X. Hong, T. Ishihara, A. V. Nurmikko, *Phys. Rev. B* **1992**, *45*, 6961.
[8] J. Byun, H. Cho, C. Wolf, M. Jang, A. Sadhanala, R. H. Friend, H. Yang, T.-W. Lee, *Adv. Mater.* **2016**, *28*, 7515.
[9] S. Aharon, B.-E. Cohen, L. Etgar, *J. Phys. Chem. C* **2014**, *118*, 17160.
[10] D. H. Cao, C. C. Stoumpos, O. K. Farha, J. T. Hupp, M. G. Kanatzidis, *J. Am. Chem. Soc.* **2015**, *137*, 7843.
[11] L. N. Quan, M. Yuan, R. Comin, O. Voznyy, E. M. Beauregard, S. Hoogland, A. Buin, A. R. Kirmani, K. Zhao, A. Amassian, D. H. Kim, E. H. Sargent, *J. Am. Chem. Soc.* **2016**, *138*, 2649.
[12] B. Cai, Y. Xing, Z. Yang, W.-H. Zhang, J. Qiu, *Energy Environ. Sci.* **2013**, *6*, 1480.
[13] E. Edri, S. Kirmayer, D. Cahen, G. Hodes, *J. Phys. Chem. Lett.* **2013**, *4*, 897.
[14] E. Edri, S. Kirmayer, M. Kulbak, G. Hodes, D. Cahen, *J. Phys. Chem. Lett.* **2014**, *5*, 429.
[15] N. Arora, S. Orlandi, M. I. Dar, S. Aghazada, G. Jacopin, M. Cavazzini, E. Mosconi, P. Gratia, F. De Angelis, G. Pozzi, M. Graetzel, M. K. Nazeeruddin, *ACS Energy Lett.* **2016**, *1*, 107.
[16] R. Sheng, A. Ho-Baillie, S. Huang, S. Chen, X. Wen, X. Hao, M. A. Green, *J. Phys. Chem. C* **2015**, *119*, 3545.
[17] H. B. Kim, I. Im, Y. Yoon, S. D. Sung, E. Kim, J. Kim, W. I. Lee, *J. Mater. Chem. A* **2015**, *3*, 9264.
[18] S. Ryu, J. H. Noh, N. J. Jeon, Y. C. Kim, W. S. Yang, J. w. Seo, S. I. Seok, *Energy Environ. Sci.* **2014**, *7*, 2614.
[19] A. Dymshits, A. Rotem, L. Etgar, *J. Mater. Chem. A* **2014**, *2*, 20776.
[20] M. Kulbak, D. Cahen, G. Hodes, *J. Phys. Chem. Lett.* **2015**, *6*, 2452.
[21] J. H. Heo, D. H. Song, S. HyukIm, *Adv. Mater.* **2014**, *26*, 8179.
[22] T. Ishihara, *J. Lumin.* **1994**, *60–61*, 274.
[23] N. Sestu, M. Cadelano, V. Sarritzu, F. Chen, D. Marongiu, R. Piras, M. Mainas, F. Quochi, M. Saba, A. Mura, G. Bongiovanni, *J. Phys. Chem. Lett.* **2015**, *6*, 4566.
[24] R. Elliott, *Phys. Rev.* **1957**, *108*, 1384.
[25] C. C. Stoumpos, D. H. Cao, D. J. Clark, J. Young, J. M. Rondinelli, J. I. Jang, J. T. Hupp, M. G. Kanatzidis, *Chem. Mater.* **2016**, *28*, 2852.
[26] S. Aharon, S. Gamliel, B. E. Cohen, L. Etgar, *Phys. Chem. Chem. Phys* **2014**, *16*, 10512.
[27] B.-E. Cohen, S. Gamliel, L. Etgar, *APL Mater.* **2014**, *2*, 081502.
[28] D. B. Mitzi, D. R. Medeiros, P. R. L. Malenfant, *Inorg. Chem.* **2002**, *41*, 2134.
[29] D. B. Mitzi, S. Wang, C. A. Field, C. A. Chess, A. M. Guloy, *Science* **1995**, *267*, 1473.
[30] N. W. Duffy, L. M. Peter, R. M. G. Rajpakshe, K. G. U. Wijayantha, *Electrochem. Commun.* **2000**, *2*, 658.